Snapshot photoacoustic topography through an ergodic relay for high-throughput imaging of optical absorption

Yang Li[1,2,6], Lei Li[1,6], Liren Zhu[1,2,6], Konstantin Maslov[1], Junhui Shi[1], Peng Hu[1], En Bo[1], Junjie Yao[2,3], Jinyang Liang[1,4], Lidai Wang[2,5] and Lihong V. Wang[1]*

Current embodiments of photoacoustic imaging require either serial detection with a single-element ultrasonic transducer or parallel detection with an ultrasonic array, necessitating a trade-off between cost and throughput. Here, we present photoacoustic topography through an ergodic relay (PATER) for low-cost high-throughput snapshot wide-field imaging. Encoding spatial information with randomized temporal signatures through ergodicity, PATER requires only a single-element ultrasonic transducer to capture a wide-field image with a single laser shot. We applied PATER to demonstrate both functional imaging of haemodynamic responses and high-speed imaging of blood pulse wave propagation in mice in vivo. Leveraging the high frame rate of 2 kHz, PATER tracked and localized moving melanoma tumour cells in the mouse brain in vivo, which enabled flow velocity quantification and super-resolution imaging. Among the potential biomedical applications of PATER, wearable devices to monitor human vital signs in particular is envisaged.

Optical imaging reveals structures and molecular information in biological tissues. Tomographic optical microscopy technologies, such as confocal microscopy, multiphoton microscopy and optical coherence tomography, form an image via mechanical or optical scanning by detecting backscattered or fluorescent photons. These systems are limited in capturing fast dynamics over a large field of view (FOV) by their imaging throughput—defined as the number of pixels in the FOV multiplied by the frame rate[1–4]. At the expense of sectioning resolution, wide-field optical imaging technology achieves high-throughput snapshot imaging by employing two-dimensional (2D) optical sensor arrays[5,6]. However, these optical imaging technologies are not well suited for mapping optical absorption[7,8]. As a complementary tool, photoacoustic (PA) imaging senses optical absorption, which holds promise for a wide range of biomedical applications[9–12]. To date, most PA imaging systems require either serial detection using a single-element ultrasonic transducer or parallel detection employing an ultrasonic transducer array. While the former has a limited imaging throughput, the latter is complex and expensive[13–18].

We propose low-cost high-throughput PA imaging based on an ergodic relay (ER) coupled with a single-element ultrasonic transducer to capture a wide-field image with only a single laser shot. We refer to this technique as photoacoustic topography through an ergodic relay (PATER). Here, topography refers to projection imaging of surface and subsurface features at depths within the ~1 mm optical diffusion limit[9,19] in scattering biological tissue. The ER is ideally a waveguide that allows the sound wave from any input point to reach any output point, with distinct delay characteristics[20,21]. In PATER, the ER—as an encoder—effectively transforms each 1D depth image (A-line) into a unique temporal signal. Through the ER, PA signals from the entire imaging volume can be detected in parallel and then decoded mathematically to reconstruct a 2D projection image. Previously, Cox and Beard numerically simulated the feasibility of PA imaging based on ergodicity[22]. However, their method differs from PATER: the simulation was limited to two dimensions instead of three dimensions, the ergodicity was achieved with a closed cavity in lieu of an open waveguide, the object was located inside the cavity rather than outside the waveguide, and the image reconstruction was based on acoustic modelling instead of experimental calibration.

We showed that PATER can image up to 9,200 pixels at a frame rate of 2 kHz over a large FOV in parallel. We demonstrated in mice in vivo the ability to capture haemodynamic responses, image the propagation of blood pulse waves, and track flowing tumour cells and localize them at super-resolution.

PATER system

PATER differs from conventional PA imaging in the operating mechanism. On the one hand, optical-resolution PA microscopy (OR-PAM) focuses a short pulse of light to a diffraction-limited spot on the object to be imaged. The optical absorbers within the illuminated zone absorb light energy and convert it into heat, which subsequently results in PA wave emission due to thermoelastic expansion[23,24]. Then, a single-element focused ultrasonic transducer detects the emitted PA waves. The optical and ultrasonic foci are scanned confocally to acquire PA signals over the entire FOV. On the other hand, PA computed tomography (PACT) uses a broad light beam to illuminate the entire FOV and uses an ultrasonic
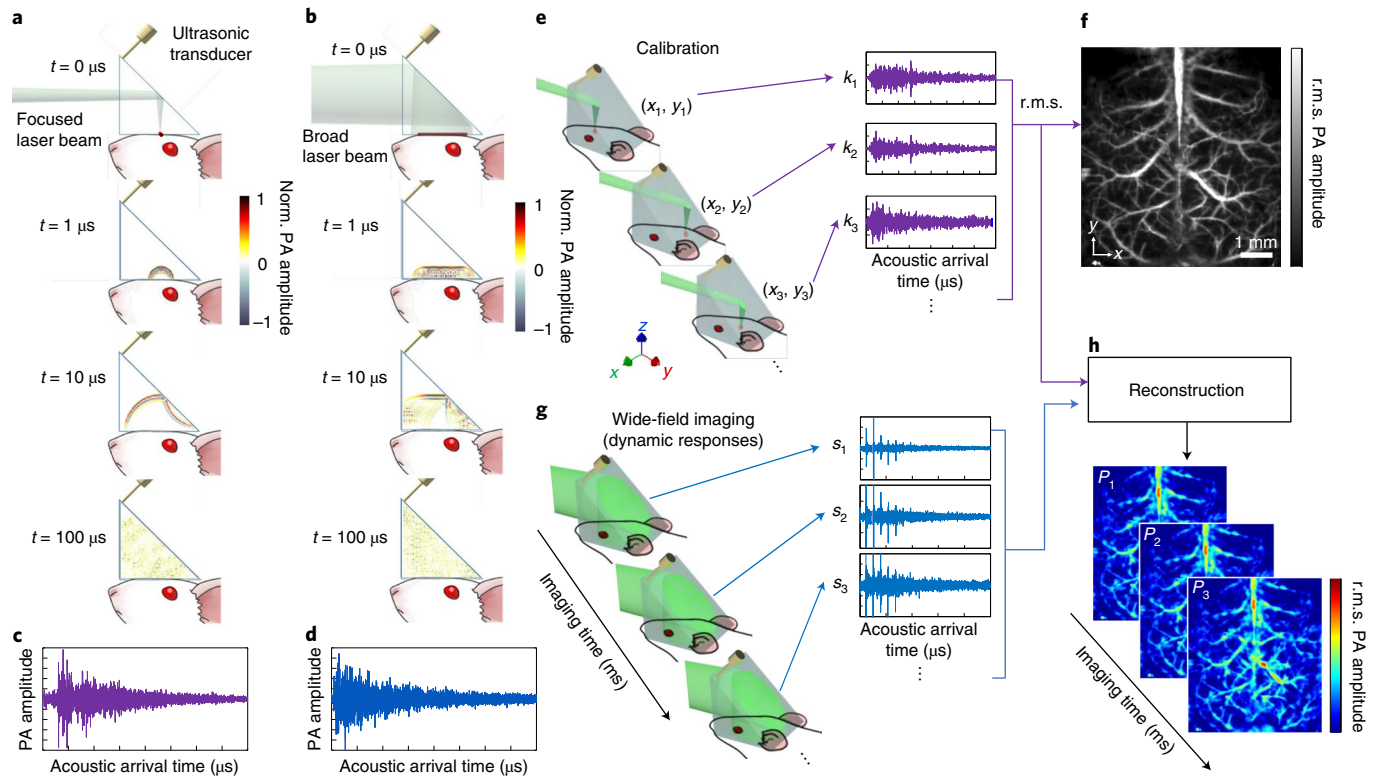
Fig. 1 | Imaging mechanism of PATER. a, Simulation of acoustic propagation in the ER in calibration mode. Norm., normalized. **b**, Simulation of acoustic propagation in the ER in wide-field mode. **c**, PA signals detected by a point detector from the simulation in **a**, with an acquisition time of 164 µs. **d**, PA signals detected by a point detector from the simulation in **b**, with an acquisition time of 164 µs. **e**, In calibration mode, light is focused on each pixel to acquire the impulse response encoded by the ER, k_i, then raster scanned over the FOV. **f**, Calibration image formed by r.m.s. projection along each A-line. **g**, Snapshot wide-field imaging. A broad laser beam illuminates the entire FOV to acquire encoded signals, s, which can be repeated for high-speed imaging. **h**, Reconstructed wide-field images. The reconstruction algorithm uses calibrated impulse responses to decode the wide-field signals and then display wide-field images.

transducer array to receive the PA waves from different angles in parallel. The detected signals are then used to form a wide-field image through digital reconstruction. In contrast, PATER uses broad light illumination but only a single-element unfocused ultrasonic transducer to acquire a snapshot wide-field image without scanning. The PA waves from the entire FOV are encoded by the ER and then are decoded through the calibrated impulse responses to yield a wide-field image (Supplementary Video 1). PATER produces 2D projection images of 3D objects, where each pixel represents the root-mean-squared (r.m.s.) projection of an A-line.

The acoustic ER is a key enabling element for PATER. To generate a distinct time-of-arrival signature for each pixel, a perfect ER entails high acoustic reflectivity at its boundaries, low acoustic attenuation inside the relay, and stringent geometric asymmetry about the contact position of the ultrasonic transducer; in addition, optical transparency is required for PATER. A right-angle prism, made of UV fused silica, has the desired optical and acoustic properties (see Methods). An unfocused pin ultrasonic transducer is placed at a corner of the prism to break the symmetry. The distinction among the time-of-arrival signatures is quantified by cross-correlating the encoded signals (Supplementary Fig. 1). Cross-correlation is found to be strong only among pixels within the acoustic diffraction limit, ~1/2 of the 250 µm acoustic wavelength. The minimal cross-correlation outside this limit indicates high distinction or low crosstalk among the pixels, which is desired for optimal spatial resolution in wide-field imaging.

PATER operates in two modes. The first, referred to as the calibration mode, focuses the laser illumination for point-by-point scanning. The second, referred to as the wide-field mode, broadens

the laser illumination for snapshot imaging. A simulation based on the k-wave toolbox[25] illustrates the imaging mechanism of PATER (Fig. 1a–d and Supplementary Video 1). An acoustic point detector is placed at a top corner opposite the square illumination face of the ER prism (Fig. 1a,b), and the detected PA signals from the two modes are shown in Fig. 1c,d.

In calibration mode, the laser beam is focused through the prism. Because the pulse width of the laser beam (~5 ns) is much shorter than the central period of the ultrasonic transducer (50 µs), and the focused beam spot (~5 µm) is much smaller than the central acoustic wavelength, the PA wave input to the PATER system can be approximated as a spatiotemporal delta function. Consequently, each calibration measurement quantifies the impulse response of the system at one pixel. The impulse responses over the entire FOV are acquired by raster scanning the focus (Fig. 1e). Unlike OR-PAM, PATER's acoustic propagation is scrambled by the ER (Supplementary Fig. 1d,e). As a result, maximum amplitude projection that is usually applied in OR-PAM does not form an accurate image of the object in PATER. Instead, we compute the r.m.s. amplitude of each received PA signal to form a projection along the A-line (Fig. 1f). The projection image acquired in this mode is called a calibration image.

In the wide-field mode, the object is uniformly illuminated by a wide-field laser beam through an engineered diffuser. The PA signals from the entire FOV are recorded in parallel, permitting snapshot wide-field imaging at a high frame rate (Fig. 1g). PATER solves an inverse problem to form a wide-field image (see Methods).

The experimental PATER system is shown in Fig. 2. While Fig. 2a shows the wide-field mode, for calibration, the diffuser
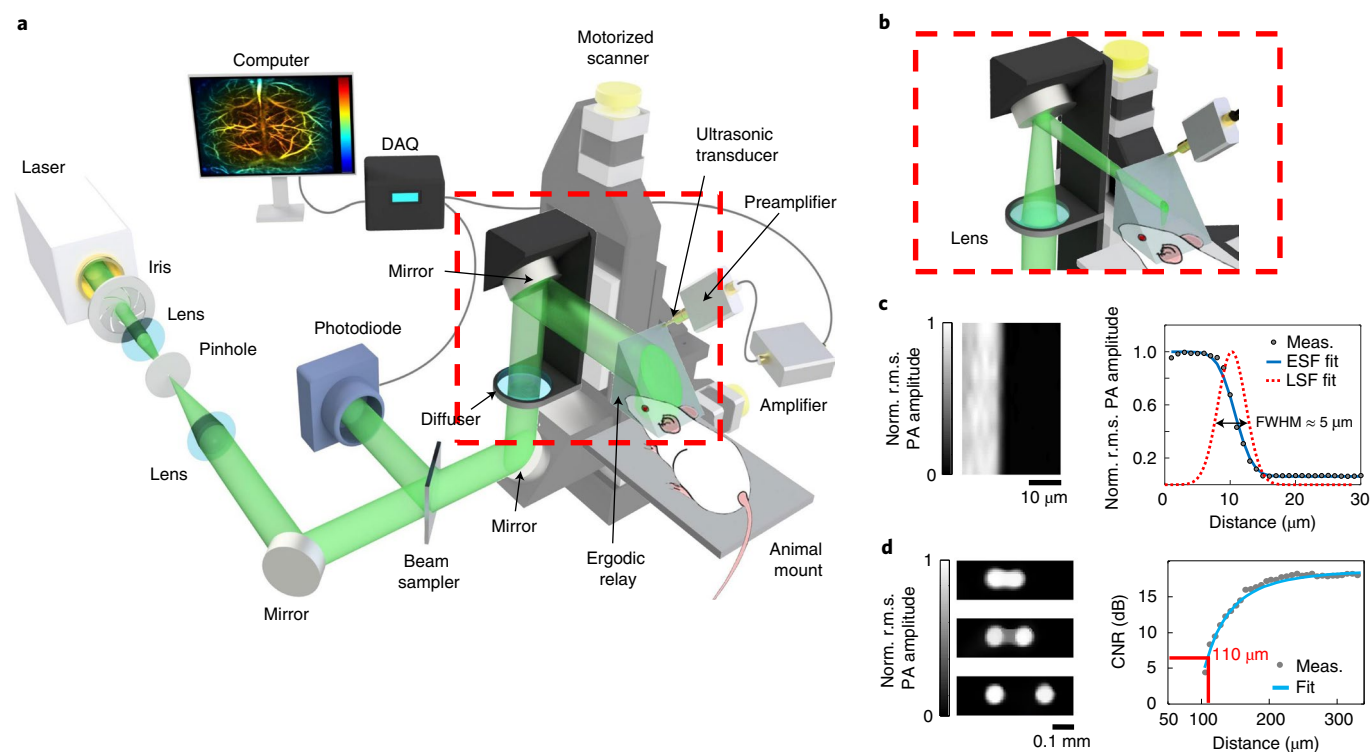
Fig. 2 | Schematic of the PATER system. a, Schematic of the wide-field mode. A diffuser creates uniform light illumination on the FOV. DAQ, data acquisition unit. **b**, Schematic of the calibration mode. The light is focused by a lens. **c**, Quantification of lateral resolution in calibration mode. The r.m.s. amplitude projection of a sharp edge is shown (left). The normalized fitted ESF is used to calculate the LSF of the system (right); the FWHM of the fitted LSF is approximately 5 μm. Norm., normalized. **d**, Quantification of lateral resolution in wide-field mode. Two light spots were shone on a black sheet. While one spot was held stationary, the other spot was translated linearly away from the first (left). The CNR versus the distance between the two spots (right) shows the lateral resolution, measured as the distance at 6 dB CNR, is 110 μm.

shown in the red dashed box is replaced with a focusing lens, as shown in Fig. 2b. For snapshot wide-field imaging, PATER has reached a high frame rate of 2 kHz, at present limited by the laser repetition rate. We quantified the lateral resolution in both calibration and wide-field modes.

In calibration mode, we imaged the edge of a sharp metal blade (Fig. 2c). Under the assumption that the beam profile was Gaussian, the r.m.s. PA amplitude averaged along the blade edge was fitted to an error function to estimate the edge-spread function (ESF). We then calculated the line-spread function (LSF) of the system by taking the derivative of the ESF. The lateral resolution, measured as the full-width at half-maximum (FWHM) of the LSF, was 5 μm, matching the diameter of the focused laser spot.

In wide-field mode, a black acrylic sheet was placed on the illumination face of the ER prism to provide uniform absorption. Two 5-μm-diameter beams were shone on the sheet. While one beam was held stationary, the second beam was translated linearly away from the first. At the same time, wide-field images were taken (Supplementary Video 2). We then calculated the contrast-to-noise ratio (CNR) versus the distance between the two beam spots (Fig. 2d). The lateral resolution, measured as the distance at 6 dB CNR, was 110 μm, approximately equal to 1/2 of the acoustic wavelength in fused silica at the ultrasonic transducer's central frequency.

Imaging mouse brain haemoglobin responses to front-paw stimulations

Snapshot imaging of fast dynamics without motion artefacts at low cost is a key advantage of PATER. First, we imaged blood flow ex vivo through biological tissue in a controlled setting as an experimental validation (Supplementary Fig. 2 and Supplementary Video 3) and

evaluated the reconstruction artefacts due to incomplete calibration (Supplementary Fig. 3). Next, we imaged in vivo the haemoglobin responses in a mouse brain to front-paw stimulations (repeated in six mice). Light at 532 nm wavelength, an approximately isosbestic wavelength for oxy- and deoxyhaemoglobin, was used for illumination. In calibration mode, the mouse brain vasculature was imaged through the intact skull but with the scalp removed (Fig. 3a, 320×240 pixels, 100-time averaging, 60-min acquisition time). In wide-field mode, the same FOV was imaged while the left and right paws were alternatingly stimulated approximately 1 s at a time by nipping with pointed forceps. The resulting wide-field images (Fig. 3b) were used to calculate the differential images after temporal running averaging (see Methods). The differential images were then overlaid onto the calibration image (Fig. 3c and Supplementary Video 4).

We observed an increase in r.m.s. PA amplitude between the two hemispheres, which was likely to be from the sagittal sinus region underneath the skull. We also observed both an increase in the contralateral somatosensory region during stimulations and a weaker increase in the ipsilateral somatosensory region (Fig. 3d,e). These increases suggest a vascular interconnection between the left and right hemispheres of the brain[26,27].

To demonstrate the maximum imaging depth, we used 1,064 nm illumination to non-invasively image blood vessels as deep as 1.1 mm in a mouse brain through an intact scalp and skull (Supplementary Fig. 4), which was validated using OR-PAM[28,29].

High-speed in vivo quantification of blood pulse wave velocity

Blood pulse wave velocity (PWV) is an important physiological parameter that characterizes cardiovascular disease progression
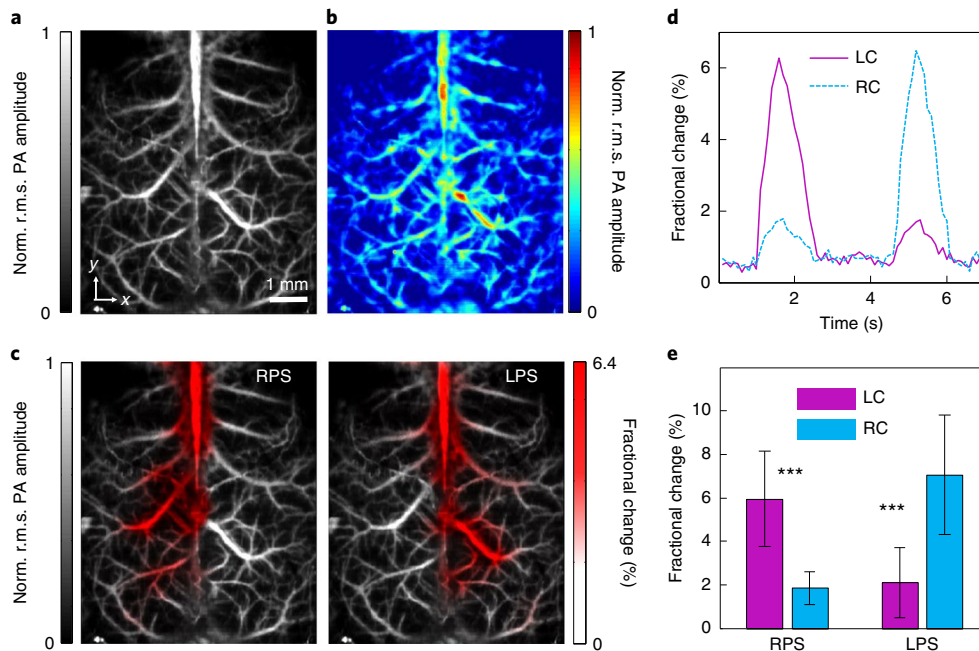
Fig. 3 | Mouse brain haemoglobin responses to front-paw stimulations. a, Calibration image of mouse brain vasculature through an intact skull. Norm., normalized. **b**, Wide-field image acquired in wide-field mode. **c**, Fractional changes in signal amplitude (shown in red) in response to right-paw stimulation (RPS, left panel) and left-paw stimulation (LPS, right panel) superimposed on the calibration image. **d**, Time courses of fractional changes in signal amplitude. LC, left cortex; RC, right cortex. **e**, Comparison of fractional changes in signal amplitude between the left and the right cortices during stimulations. Error bars, standard deviations ($N = 26 \times 25$ pixels). ***, $p < 0.001$, calculated by the two-sample t-test.
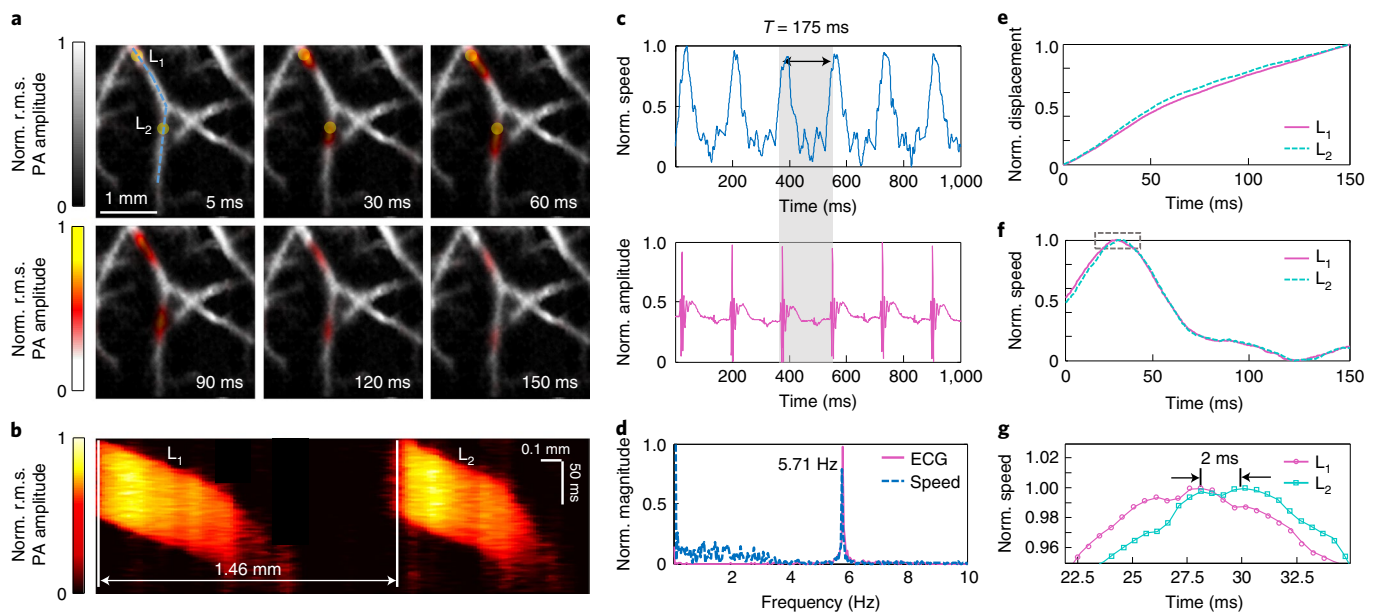

Fig. 4 | Quantification of blood pulse wave velocity. a, Wide-field images of thermal wave propagation in the middle cerebral arteries. The yellow circles, labelled L_1, L_2, indicate the locations of the laser heating spots during wide-field measurement. **b**, Space-time domain images along the blue dashed line in **a**. Norm., normalized. **c**, Blood flow speed (top) and electrocardiogram (ECG) cycles (bottom) measured at L_1. The blood flow speed oscillates periodically with the cardiac cycle. The grey region shows one cardiac cycle. **d**, Fourier transform of signals in **c**. The peaks at 5.71 Hz show the cardiac frequency. Both the ECG and blood speed measurements show the same cardiac frequency. **e**, Plot of averaged thermal wave displacement over time at spots L_1 and L_2. **f**, Plot of averaged blood flow speed calculated from **e**. **g**, Zoomed-in view of the boxed region in **f**. The delay between the two peaks is 2 ms.

associated with arterial stiffness[30,31]. Owing to the fast propagation of the pulse waves in major arteries, the quantification of PWV previously relied on either measuring the blood flow speed at two distant sites or quantifying the cross-covariance of flow patterns[32,33],

methods that were indirect and prone to errors. With PATER's high imaging speed, we demonstrated in mice ($n = 4$) in vivo the measurement of blood flow speed at multiple sites simultaneously and mapped the PWV in the arterial network.
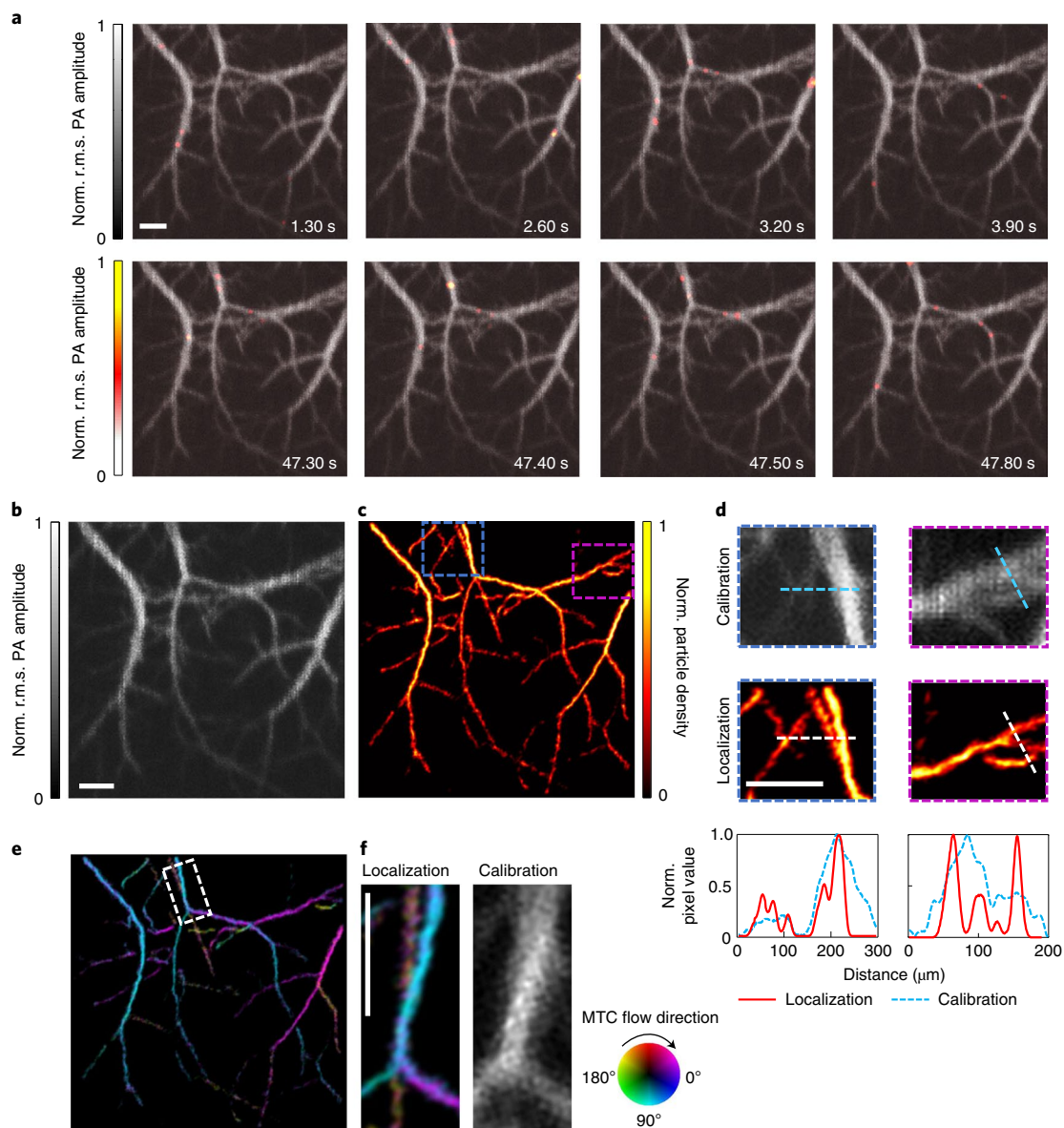
Fig. 5 | Localization and tracking of MTCs in the mouse brain at super-resolution. a, Tracking of MTC flow over time, where the red spots highlight the migrating tumour cells in the current frame and grey shows the calibration image. Norm., normalized. **b**, Calibration image of the mouse brain vasculature. **c**, Localization map of the mouse brain vasculature reconstructed by superimposing the tracked MTC positions from all frames. **d**, Zoomed-in views of the coloured boxed regions from **c** versus the same regions from **b**. The profiles across the dashed lines are plotted at the bottom. **e**, Flow direction map of the MTCs overlaid on the localization map. **f**, Zoomed-in view of the boxed region from **e**. The opposite flow directions of the neighbouring vessels (left panel) are differentiated in the super-resolution but not in the calibration image (right panel). All scale bars, 250 μm.

After calibration (200 × 200 pixels, 100-time averaging, 30-min acquisition time), wide-field measurements on a cerebral region of the mouse brain were taken to image the blood flow in the middle cerebral arteries (MCAs). A laser diode generated multiple confined heating spots on the MCAs during the wide-field measurements (see Methods). The wide-field images show that thermal waves propagate with the blood flow in the MCAs (Fig. 4a and Supplementary Video 5).

A branch of the MCAs shown by the dotted blue line in Fig. 4a was segmented to analyse the propagation of thermal waves over time (Fig. 4b). Here the thermal conduction is negligible, so the thermal wave propagation speed approximates the blood flow speed. The blood flow speed at each heating spot was calculated from the space-time images (Fig. 4b and Methods). Owing to the pulse wave propagation, the blood flow speed in the MCAs

fluctuates over time. Figure 4c,d shows that the blood flow speed changes periodically and that the period aligns well with the cardiac cycle recorded by electrocardiography.

The heat propagation displacement from the two heating spots over time, averaged over 50 cardiac cycles, is plotted in Fig. 4e. The averaged flow speed was calculated by taking the first derivative of the displacement over time (Fig. 4f). The side lobes, after the main lobes, are possibly due to the cushioning effect of arteries or reflected waves from any point of structural discontinuity in the arterial tree[31]. The delay time was quantified by calculating the lag between the main lobes' peaks (Fig. 4g). The distance between the two heating spots (L_1 and L_2) was 1.46 mm (Fig. 4b). The PWV was computed by taking the ratio of the distance between the heating spots to the delay time. The quantified PWV was ~0.73 m s^{-1}, which falls within the range of literature-reported values[32,34]. Taking

advantage of PATER's high imaging speed, a PWV map of the MCA network was constructed by imaging the blood flow at multiple sites simultaneously (Supplementary Fig. 5).

Tracking and localizing flowing melanoma cells in vivo to image vasculature at super-resolution

The presence of circulating tumour cells is a key determinant of tumour metastasis, the spread of cancer cells from a primary site to distant organs that leads to the growth of new tumours[35,36]. Most melanoma tumour cells (MTCs) contain high concentrations of melanin. The much stronger optical absorption of melanin than haemoglobin around 660 nm (Supplementary Fig. 6a) provides a large optical contrast between the circulating tumour cells and the background blood. In this study, we injected MTCs both in vitro and in vivo in mice to simulate circulating tumour cells.

If the imaged MTCs are sufficiently separated in a wide-field image (that is, at most one single cell or cell cluster within a resolution voxel at a time), we can localize each individual cell or cell cluster. The localization error (quantified by the r.m.s. error of the fitted centre position of a single melanoma cell) is inversely proportional to the signal-to-noise ratio (SNR; Supplementary Note 1), which enables super-resolution imaging (see Methods, Supplementary Fig. 6b–d and Supplementary Video 6). Although published after our manuscript submission, an independent in vitro demonstration of localization based on conventional PACT[37] with non-biological particles is acknowledged here.

In our study, we demonstrated super-resolution imaging of the mouse brain vasculature in vivo by localizing and recording the positions of MTCs without labelling. Although the MTCs moved slowly in absolute speed (~0.5 mm s^{-1}, Supplementary Note 2), they actually moved fast on a super-resolution basis, that is, the cells displaced 1/2 of the super-resolution pixel width (300 nm/2) over a short time interval. To capture the minute displacement accurately, high frame rates on the order of kilohertz were required. The particle density of the localization-enhanced vessels depended on the number of trackable MTCs. Therefore, vessels traced with more MTC events could be more densely sampled.

After calibration (200 × 200 pixels, 100-time averaging, 30-min acquisition time), wide-field measurements on a cortical region of the mouse brain were taken upon the injection of MTCs through the mouse's carotid artery (see Methods). The wide-field images (with a threshold of 20% from the global maximum, Fig. 5a and Supplementary Videos 7 and 8) were overlaid onto the calibration image (Fig. 5b) to highlight the current positions of MTCs. Owing to the scattering of the skull, the resolution of the calibration image is 25 µm (Supplementary Fig. 7a), worse than the resolution of 5 µm in a clear medium.

The localized positions of the MTCs from 200,000 wide-field images were computed to reconstruct a localization map of the high-resolution cortical vasculature (Fig. 5c and Supplementary Video 9). The localization map provided finer resolution than the calibration image, resolving the vessels at the bifurcations boxed in Fig. 5c (Fig. 5d). The line profiles across the vessels showed that two neighbouring vessels branching out from each other were separated at a distance as small as 12 µm, and the FWHM for one of the smallest vessels shown was 7 µm (Supplementary Fig. 7b), which falls in the range of diameters of capillaries (5–10 µm). The finest resolution, quantified from two traces of MTCs migrating through two crossed blood vessels, was 300 nm (see Methods, Supplementary Figs. 7c,d and 8, and Supplementary Note 1).

The tumour cell flow directions in the vessels were analysed (Fig. 5e). The differences in flow direction (Fig. 5f) and speed (Supplementary Fig. 9 and Supplementary Note 2) among closely neighbouring vessels enabled differentiation while they could not be resolved in the calibration images.

Discussion

Photoacoustic imaging technology has unique advantages in sensing optical absorption contrast of molecules in biological tissue, but has never before been developed into an imaging modality that combines snapshot, high frame rate, wide FOV and low cost into a single system. PATER has overcome these limitations by employing an acoustic ER to encode the PA waves from a 3D volume to 1D temporal signals. Each wide-field image is acquired within the acoustic transit time—164 µs at the current centre ultrasonic frequency, avoiding motion artefacts altogether. According to the transit time, PATER can theoretically reach a frame rate up to 6 kHz over the largest experimentally demonstrated FOV of 8 × 6 mm², both of which are expected to scale with the centre ultrasonic frequency. Even the current 2 kHz imaging speed is much higher than that of either scanning-based single-transducer PA microscopy[17,26,38], or array-based PA imaging[13,39,40] systems over a similar FOV. PATER facilitates imaging of fast dynamic activities in vivo and promises many biomedical applications—such as quantifying the stiffness of blood vessels via measuring PWV, imaging of the responses of voltage or calcium indicators of neural activity and high-speed clinical analysis of histological tissues. Lastly, PATER's single-channel ultrasonic detection greatly reduces the size, complexity and cost of the system compared with a multichannel counterpart.

The current calibration method limits PATER to detect dynamics from regions that exhibited high absorption during calibration, and features that show up after calibration may not be accurately represented. In addition, the present embodiment of PATER operates at depths within the optical diffusion limit and requires calibration for each object. Overcoming these limitations would empower the technique further. PATER is expected to be suitable for portable applications, such as using a wearable device to monitor vital signs.

Online content

Any methods, additional references, Nature Research reporting summaries, source data, extended data, supplementary information, acknowledgements, peer review information; details of author contributions and competing interests; and statements of data and code availability are available at https://doi.org/10.1038/s41566-019-0576-2.

References

1. Juskaitis, R., Wilson, T., Neil, M. M. A. & Kozubek, M. Efficient real-time confocal microscopy with white light sources. *Nature* **383**, 804–806 (1996).
2. Denk, W., Strickler, J. H. & Webb, W. W. Two-photon laser scanning fluorescence microscopy. *Science* **248**, 73–76 (1990).
3. Horton, N. G. et al. In vivo three-photon microscopy of subcortical structures within an intact mouse brain. *Nat. Photon.* **7**, 205–209 (2013).
4. Vakoc, B. J., Fukumura, D., Jain, R. K. & Bouma, B. E. Cancer imaging by optical coherence tomography: preclinical progress and clinical potential. *Nat. Rev. Cancer* **12**, 363–368 (2012).
5. Etoh, T. G. et al. An image sensor which captures 100 consecutive frames at 1000000 frames/s. *IEEE Trans. Electron. Dev.* **50**, 144–151 (2003).
6. Gao, L., Liang, J., Li, C. & Wang, L. V. Single-shot compressed ultrafast photography at one hundred billion frames per second. *Nature* **516**, 74–77 (2014).
7. Wu, H. et al. Eulerian video magnification for revealing subtle changes in the world. *ACM Trans. Graphics* **31**, 1–8 (2012).
8. Bouchard, M. B., Chen, B. R., Burgess, S. A. & Hillman, E. M. C. Ultra-fast multispectral optical imaging of cortical oxygenation, blood flow, and intracellular calcium dynamics. *Opt. Express* **17**, 15670–15678 (2009).
9. Wang, L. V. & Hu, S. Photoacoustic tomography: in vivo imaging from organelles to organs. *Science* **335**, 1458–1462 (2012).
10. Jathoul, A. P. et al. Deep in vivo photoacoustic imaging of mammalian tissues using a tyrosinase-based genetic reporter. *Nat. Photon.* **9**, 239–246 (2015).
11. Taruttis, A. & Ntziachristos, V. Advances in real-time multispectral optoacoustic imaging and its applications. *Nat. Photon.* **9**, 219–227 (2015).

12. Wang, L. V. & Yao, J. A practical guide to photoacoustic tomography in the life sciences. *Nat. Methods* **13**, 627–638 (2016).

13. Li, L. et al. Single-impulse panoramic photoacoustic computed tomography of small-animal whole-body dynamics at high spatiotemporal resolution. *Nat. Biomed. Eng.* **1**, 0071 (2017).

14. Deán-Ben, X. L. & Razansky, D. Adding fifth dimension to optoacoustic imaging: volumetric time-resolved spectrally enriched tomography. *Light Sci. Appl.* **3**, e137 (2014).

15. Yao, J. et al. Multiscale photoacoustic tomography using reversibly switchable bacterial phytochrome as a near-infrared photochromic probe. *Nat. Methods* **13**, 67–73 (2015).

16. Gamelin, J. et al. A real-time photoacoustic tomography system for small animals. *Opt. Express* **17**, 10489–10498 (2009).

17. Wong, T. T. W. et al. Label-free automated three-dimensional imaging of whole organs by microtomy-assisted photoacoustic microscopy. *Nat. Commun.* **8**, 1386 (2017).

18. Li, L. et al. Label-free photoacoustic tomography of whole mouse brain structures ex vivo. *Neurophotonics* **3**, 035001 (2016).

19. Wang, L. V. Multiscale photoacoustic microscopy and computed tomography. *Nat. Photon.* **3**, 503–509 (2009).

20. Draeger, C. & Fink, M. One-channel time reversal of elastic waves in a chaotic 2D-silicon cavity. *Phys. Rev. Lett.* **79**, 407–410 (1997).

21. Ing, R. K., Quieffin, N., Catheline, S. & Fink, M. In solid localization of finger impacts using acoustic time-reversal process. *Appl. Phys. Lett.* **87**, 204104 (2005).

22. Cox, B. & Beard, P. C. Photoacoustic tomography with a single detector in a reverberant cavity. *J. Acoustical Soc. Am.* **125**, 1426–1436 (2009).

23. Wang, L. V. Photo acoustic tomography. *Scholarpedia* **9**, 10278 (2014).

24. Beard, P. C. Biomedical photoacoustic imaging. *Interface Focus* **1**, 602–631 (2011).

25. Treeby, B. & Cox, B. k-Wave: MATLAB toolbox for the simulation and reconstruction of photoacoustic wave-fields. *J. Biomed. Opt.* **15**, 021314 (2010).

26. Yao, J. et al. High-speed label-free functional photoacoustic microscopy of mouse brain in action. *Nat. Methods* **12**, 407–410 (2015).

27. Liao, L. D. et al. Transcranial imaging of functional cerebral hemodynamic changes in single blood vessels using in vivo photoacoustic microscopy. *J. Cerebral Blood Flow Metabolism* **2**, 938–951 (2012).

28. Hai, P., Yao, J., Maslov, K., Zhou, Y. & Wang, L. V. Near-infrared optical-resolution photoacoustic microscopy. *Opt. Lett.* **39**, 5192–5195 (2014).

29. Hsu, H.-C. et al. Dual-axis illumination for virtually augmenting the detection view of optical-resolution photoacoustic microscopy. *J. Biomed. Opt.* **23**, 076001 (2018).

30. Georgianos, P. I., Pikilidou, M. I., Liakopoulos, V., Balaska, E. V. & Zebekakis, P. E. Arterial stiffness in end-stage renal disease—pathogenesis, clinical epidemiology, and therapeutic potentials. *Hypertension Res.* **41**, 309–319 (2018).

31. London, G. M. & Guerin, A. P. Influence of arterial pulse and reflected waves on blood pressure and cardiac function. *Am. Heart J.* **138**, S220–S224 (1999).

32. Yeh, C., Hu, S., Maslov, K. & Wang, L. V. Photoacoustic microscopy of blood pulse wave. *J. Biomed. Opt.* **17**, 070504 (2012).

33. Fitch, R. M., Vergona, R., Sullivan, M. E. & Wang, Y.-X. Nitric oxide synthase inhibition increases aortic stiffness measured by pulse wave velocity in rats. *Cardiovasc. Res.* **51**, 351–358 (2001).

34. Seki, J. Flow pulsation and network structure in mesenteric microvasculature of rats. *Am. J. Physiol. Heart Circulatory Physiol.* **266**, H811–H821 (1994).

35. Miura, G. Cancer tumor imaging: catch me if you can. *Nat. Chem. Biol.* **10**, 485 (2014).

36. Hai, P. et al. Label-free high-throughput detection and quantification of circulating melanoma tumor cell clusters by linear-array-based photoacoustic tomography. *J. Biomed. Opt.* **22**, 041004 (2017).

37. Dean-Ben, X. L. & Razansky, D. Localization optoacoustic tomography. *Light Sci. Appl.* **7**, 18004 (2018).

38. Liang, Y., Jin, L., Guan, B.-O. & Wang, L. 2 MHz multi-wavelength pulsed laser for functional photoacoustic microscopy. *Opt. Lett.* **42**, 1452–1455 (2017).

39. Li, L. et al. Small near-infrared photochromic protein for photoacoustic multi-contrast imaging and detection of protein interactions in vivo. *Nat. Commun.* **9**, 2734 (2018).

40. Wu, Z. et al. A microrobotic system guided by photoacoustic computed tomography for targeted navigation in intestines in vivo. *Sci. Robot.* **4**, eaax0613 (2019).

Methods

System set-up. A 5 ns pulsed laser beam at 532 nm (INNOSAB IS8II-E, Edgewave GmbH; 2 kHz pulse repetition rate) was partially reflected by a beam sampler to a photodiode (DET36A, Thorlabs, Inc.) to correct PA signals for fluctuations in light energy. The laser beam that passed through the beam splitter was reflected by a mirror (PF10-03-P01, Thorlabs, Inc.) and passed through a lens (LA1509, Thorlabs, Inc.; 2.54 cm diameter and 100 mm focal length) or an engineered diffuser (EDC-5-A-1r, RPC Photonics, Inc.; 5.5° divergence angle) in the light path according to the acquisition mode (Fig. 2a,b).

A two-channel digitizer (ATS9350, AlazarTech, Inc.; 12 bits, 100 megasamples per second sampling rate, and 16,384 data points per acquisition sampling length) was used to record the PA signal and the photodiode output.

Acoustic ER. A right-angle prism made of UV fused silica (PS615, Thorlabs, Inc.; 1.5 cm right-angle edge length, 2,203 kg m^{-3} density and 73.6 GPa Young's modulus) was chosen to serve as the acoustic ER. It has a 99.99% normal-incidence acoustic reflectivity by amplitude at the boundary between the prism and air. The acoustic attenuation coefficient is approximately 2.4 nepers m^{-1} at 20 MHz, indicating negligible attenuation in the prism over the detectable path-length range[41]. An unfocused pin ultrasonic transducer (VP-0.5-20 MHz, CTS Electronics, Inc.; 20 MHz central frequency, 56% one-way bandwidth and 0.5 mm element size) was placed at a corner of the prism to avoid symmetry. To facilitate the transmission of PA waves using ultrasound coupling media, ultrasound gel was applied between the object and the prism, while polyester resin was added between the prism and the ultrasonic transducer (Fig. 2a).

Tunable laser. A tunable dye laser (CBR-D, Sirah GmbH), using 4-(dicyanomethylene)-2-methyl-6-(4-dimethylaminostyryl)-4H-pyran dissolved in ethanol as the gain medium, was pumped by a 532 nm pulsed laser to generate a laser beam at 660 nm wavelength for monitoring MTC migrations in the mouse brain. The fluence of the laser beam in wide-field mode was ~2 mJ cm^{-2} (10 mJ maximum pulse energy from the Edgewave INNOSAB IS8II-E pump laser, 20% efficiency of the dye laser at 660 nm and ~1 cm^2 area of illumination), which was well below the ANSI safety limit[42].

Image reconstruction. Each wide-field measurement can be expressed as a linear combination of the impulse responses from all pixels:

$$s(t) = \sum_{i=1}^{N_p} k_i(t)P_i \qquad (1)$$

where s denotes the received wide-field PA signal, t time, i the pixel index, N_p the total number of pixels, k_i the normalized impulse response from the calibration and P_i the r.m.s. PA amplitude. The r.m.s. value of the raw calibration signal $\tilde{k}_i(t)$ for the ith pixel was calculated as

$$\text{r.m.s.}_i = \sqrt{\frac{1}{N_t}\sum_{j=1}^{N_t}\left[\tilde{k}_i(t_j)\right]^2} \qquad (2)$$

where N_t denotes the number of sampled time points and t time. A 2D density plot of r.m.s.$_i$ over all pixels is a calibration image. To construct the system matrix K, the normalized impulse response was computed for each time point through $k_i(t_j) = \tilde{k}_i(t_j)/\text{r.m.s.}_i$.

Once time t is discretized according to the Nyquist criterion, equation (1) can be recast to matrix form:

$$\mathbf{s} = K\mathbf{P} \qquad (3)$$

where $K = [k_1, k_2, \ldots, k_{N_p}]$ is the system matrix. The wide-field image $\mathbf{P}$ (Fig. 1h) is reconstructed from the signal $\mathbf{s}$ by solving the inverse problem of equation (2).

A two-step iterative shrinkage/thresholding (TwIST) algorithm[43] was implemented to solve equation (2) for $\mathbf{P}$ as a minimizer of the objective function:

$$\hat{\mathbf{P}} = \arg\min_{\mathbf{P}}||\mathbf{s} - K\mathbf{P}||^2 + 2\lambda\Phi_{TV}(\mathbf{P}) \qquad (4)$$

Here $\Phi_{TV}(\mathbf{P})$ is the total variation reg ularization term and λ is the regularization parameter. A single 2D PATER image takes ~15 s to reconstruct on a typical workstation (Intel Xeon E5-2620v2, 2.10 GHz, 8 cores and 16 GB RAM).

The maximum number of resolvable pixels, N, from the reconstructed image is approximately 14,000 pixels (Supplementary Note 3). Given the wide-field imaging resolution of 110 μm (as shown in Fig. 2d), PATER's reconstruction pixel size was chosen at 50 μm, that is, ~1/2 of the resolution. With an image FOV of 8×6 mm^2, we have 160×120 = 19,200 pixels, where ~48% pixels had r.m.s. values higher than twice (6 dB) the noise r.m.s. amplitude. Thus, the number of active resolvable pixels in the image is 19,200×48% = 9,200. Given the same illumination fluence (mJ cm^{-2}) between point-by-point scanning imaging and wide-field imaging, the expected SNR values of the two measurements are approximately the same (Supplementary Note 4).

To avoid computational instability and to ensure image quality, we used the r.m.s. values to select pixels to form the system matrix. Pixels with r.m.s. values lower than twice (6 dB) the noise amplitude were considered as the background that was too dark to calibrate for; therefore, the impulse responses of these pixels were excluded from the system matrix K. This initial check ensured that only foreground pixels with sufficient SNRs were considered in the reconstruction. This approach holds valid if, during the experiment, no detectable absorber appears in the background pixels.

In vitro study of blood flow behind biological tissue. An ~1-mm-thick layer of chicken breast tissue was placed between the ER and two parallel rubber tubes with 0.6 mm inner diameters. The tubes were filled with blood for calibration. During wide-field imaging, the blood in one tube was flushed out with distilled water, while the blood in the other tube was held stationary (Supplementary Fig. 2).

Experimental animals. We used female ND4 Swiss Webster mice (Envigo; 18–20 g and 6–8 weeks old) for the in vivo studies. All the laboratory animal protocols were approved by the Animal Studies Committee of Washington University in St. Louis and the Institutional Animal Care and Use Committee of California Institute of Technology. For imaging, the mouse was anaesthetized in a small chamber with 5% vaporized isoflurane mixed with air for anaesthesia induction, and then transferred to a customized animal mount where the mouse was kept anaesthetized with a continuous supply of 1.5% vaporized isoflurane. The animal mount consisted of a stereotaxic frame that fixed the mouse's head, and a heating pad that maintained the mouse's body temperature at ~38 °C. The hair on the mouse's head was razor trimmed, and the scalp was either kept intact or surgically removed, depending on the experiment, but the skull was always left intact. Bloodstains on the skull were carefully cleaned with phosphate-buffered saline solution, and ultrasound gel was applied on the skull as an acoustic coupling medium. Then, the animal mount was raised until the mouse's skull was in contact with the illumination face of the ER prism. An adequate amount of pressure was maintained between the mounted animal and the ER to prevent the mouse's head from moving, but not so much pressure as to interrupt the blood supply in the brain.

Differential measurement calculation. Differences in wide-field measurements were calculated as follows:

$$\Delta\mathbf{P}_j = \frac{\sum_{i=j}^{j+4}\mathbf{P}_i}{5} - \frac{\sum_{i=1}^{5}\mathbf{P}_i}{5} \qquad (5)$$

where $\mathbf{P}_i$ is the ith wide-field image and j is the frame index to the averaged images. The above temporal running averaging was applied only to the experimental analyses that are indicated in the main text. The wide-field differential images were processed in MATLAB with a 2D median filter (medfilt2) using median values from the 5-by-5 neighbourhood pixels and a 2D Gaussian filter (imgaussfit) with a sigma value of 10. Two regions of interest from each side of the mouse brain, with the same sample size of $N = 26 \times 25$ pixels, were selected for the mouse brain haemoglobin response analyses (Fig. 3d).

Laser heating. The light beam from a continuous-wave laser diode (MLL-III-532-200mW, CNI Laser; 200 mW) was passed through beam splitters (BS010, Thorlabs Inc.) and focused on to multiple spots on the vessels of interest. The positions of the heating spots were controlled by a set of mirrors. The duration and frequency of the heating cycle were controlled by a function generator (DG1022, Rigol; 5.71-Hz frequency, 40% duty cycle). Because the PA signal amplitude is dependent on temperature, the heat-induced thermal wave propagation can be measured.

Analysis of pulse wave propagation. The vessels of interest were first manually identified from the images. Time traces at points along these vessels were extracted, forming images in the space-time domain (that is, distance along the vessels versus elapsed time). The space-time domain images were processed with a threshold at 20% of maximum and interpolated to extract the flow displacement curves over time. To suppress noise, the thermal wave propagation at each heating spot was segmented and averaged based on the cardiac cycles from the ECG measurement. We assumed that thermal conduction was negligible and that the thermal wave propagation was primarily due to blood flow. The flow speed, ν, was calculated by taking the first derivative of the flow displacements with respect to time. Because the temporal resolution was 0.5 ms in our current set-up, a PWV of up to ~200 cm s^{-1} could be measured between two spots separated by ~1 mm distance.

Animal preparation for MTC injection. A carotid artery cannulation procedure[44] was performed on the mouse to access the left common carotid artery. An arterial catheter (MAC-02, SAI Infusion Technologies Inc.; 1-F tip outer diameter) was inserted into the left common carotid artery to facilitate melanoma cancer cell injection. The skins were sutured after the procedure while the arterial catheter was exposed as the tumour cell injection port.

Real-time monitoring of MTCs in the mouse brain in vivo. A cortical region of the mouse's brain was scanned for calibration after performing the carotid artery cannulation procedure. Approximately $200\,\mu l$ of cell suspension containing 3×10^6 B16 cells was slowly injected through the arterial catheter into the left common carotid artery. Then, wide-field images of the cortical region were acquired using 660 nm light to monitor the migration of MTCs for 100 s.

Localization and tracking of MTCs in vivo. While the major noise source in optical super-resolution microscopy is photon shot noise from the signal itself, PATER's noise is mainly from the medium and detector[45]. The localization error of PATER, computed using least-squares fitting to a Gaussian function[46], is defined as the r.m.s. error of the fitted centre position $\hat{x}_0$:

$$\sqrt{\langle(\Delta\hat{x}_0)^2\rangle} = 2^{3/4}\frac{\sigma}{\text{SNR}_L} \qquad (6)$$

where σ is the standard deviation of the original Gaussian point-spread function and SNR_L is the signal-to-noise ratio in a conceptual pixel of width $L = \sqrt{2\pi}\sigma$ (Supplementary Note 1 and Supplementary Fig. 8).

To track and localize MTCs over the FOV, we imaged the mouse brain at 2,000 frames per second for 100 s. In the entire 3D (x–y–t) volume, the centres of the MTCs were localized at a sub-pixel accuracy as follows: (1) suppressing noise by temporal running averaging; (2) applying a difference-of-Gaussian filter, with empirically determined scales of 1.4 and 1.8 pixels; (3) identifying all local maxima above 20% of the global maximum; and then (4) fitting a 2D Gaussian function to the neighbourhood of each local maximum. The MTCs were further filtered with the trackability criterion: over the course of the video, we kept only MTCs that were tracked in at least 3 frames within a 5-frame window and found to have a flow speed $\leq 10\,\text{m s}^{-1}$. The tracked MTCs were then connected into paths to form the localization image. The finest resolution was estimated to be 300 nm ($\sigma = 100\,\mu m$, SNR = 110 at a pixel width of $10\,\mu m$ or $\text{SNR}_L = 550.7$, super-resolution pixel size = 100 nm; Supplementary Note 1 and Supplementary Fig. 7c,d).

Mapping of flow velocity of MTCs in vivo. The major vessels were manually identified from the calibration image, and MTCs were tracked to map the flow velocity. MTC signals were extracted along the vessel centrelines from the video to form a space-time domain plot for each vessel. The moving window Fourier transformation-based flow speed extraction algorithm[13] was used to calculate the flow speed and direction along the vessels (Supplementary Fig. 9c,d).

Reporting Summary. Further information on research design is available in the Nature Research Reporting Summary linked to this article.

Data availability
The data that support the plots within this paper and other findings of this study are available from the corresponding author upon reasonable request and with permission from corporate collaborations.

Code availability
The reconstruction algorithm and data processing methods are described in detail in the Methods. We have opted not to make the computer codes publicly available owing to corporate collaborations and pending patent applications.

References
41. *Moderne Messmethoden der Physik* Vol. 1, 2, Extended edition (Deutscher Verlag der Wissenschaften, 1960).
42. Laser Institute of America. American National Standard for safe use of lasers (American National Standards Institute, 2000).
43. Bioucas-Dias, J. M. & Figueiredo, M. A. T. A new TwIST: two-step iterative shrinkage/thresholding algorithms for image restoration. *IEEE Trans. Image Processing* **16**, 2992–3004 (2007).
44. Jacobs, J. D. & Hopper-Borge, E. A. Carotid artery infusions for pharmacokinetic and pharmacodynamic analysis of taxanes in mice. *J. Vis. Exp.* **92**, e51917 (2014).
45. Winkler, A. M., Maslov, K. & Wang, L. V. Noise-equivalent sensitivity of photoacoustics. *J. Biomed. Opt.* **18**, 097003 (2013).
46. Thompson, R. E., Larson, D. R. & Webb, W. W. Precise nanometer localization analysis for individual fluorescent probes. *Biophys. J.* **82**, 2775–2783 (2002).

Author contributions
Y.L. and L.L. designed the study. Y.L., L.L. and K.M. built the imaging system. L.L. and Y.L. planned the experiments. Y.L., L.L., E.B. and J.Y. performed the experiments. J.S. and L.W. developed the data acquisition program. L.Z., Y.L. and L.L. developed the reconstruction algorithm. Y.L., L.L., L.Z., J.L., P.H. and J.Y. analysed the data. L.V.W. conceived the concept and supervised the project. All authors contributed to writing the manuscript.

Competing interests
L.V.W. and K.M. have financial interests in Microphotoacoustics, Inc., CalPACT, LLC and Union Photoacoustic Technologies, Ltd, which did not support this work.

Additional information
Supplementary information is available for this paper at https://doi.org/10.1038/s41566-019-0576-2.

Correspondence and requests for materials should be addressed to L.V.W.

Reprints and permissions information is available at www.nature.com/reprints.

nature research

Corresponding author(s): Lihong Wang

Last updated by author(s): Oct 20, 2019

Reporting Summary

Nature Research wishes to improve the reproducibility of the work that we publish. This form provides structure for consistency and transparency in reporting. For further information on Nature Research policies, see Authors & Referees and the Editorial Policy Checklist.

Statistics

For all statistical analyses, confirm that the following items are present in the figure legend, table legend, main text, or Methods section.

n/a	Confirmed	
☒	☐	The exact sample size (*n*) for each experimental group/condition, given as a discrete number and unit of measurement
☒	☐	A statement on whether measurements were taken from distinct samples or whether the same sample was measured repeatedly
☒	☐	The statistical test(s) used AND whether they are one- or two-sided *Only common tests should be described solely by name; describe more complex techniques in the Methods section.*
☒	☐	A description of all covariates tested
☒	☐	A description of any assumptions or corrections, such as tests of normality and adjustment for multiple comparisons
☒	☐	A full description of the statistical parameters including central tendency (e.g. means) or other basic estimates (e.g. regression coefficient) AND variation (e.g. standard deviation) or associated estimates of uncertainty (e.g. confidence intervals)
☒	☐	For null hypothesis testing, the test statistic (e.g. F, t, r) with confidence intervals, effect sizes, degrees of freedom and P value noted *Give P values as exact values whenever suitable.*
☒	☐	For Bayesian analysis, information on the choice of priors and Markov chain Monte Carlo settings
☒	☐	For hierarchical and complex designs, identification of the appropriate level for tests and full reporting of outcomes
☒	☐	Estimates of effect sizes (e.g. Cohen's *d*, Pearson's *r*), indicating how they were calculated

Our web collection on statistics for biologists contains articles on many of the points above.

Software and code

Policy information about availability of computer code

Data collection	LabVIEW 2015, AlazarTech ATS-VI 5.8.3
Data analysis	Matlab 2017b

For manuscripts utilizing custom algorithms or software that are central to the research but not yet described in published literature, software must be made available to editors/reviewers. We strongly encourage code deposition in a community repository (e.g. GitHub). See the Nature Research guidelines for submitting code & software for further information.

Data

Policy information about availability of data

All manuscripts must include a data availability statement. This statement should provide the following information, where applicable:

- Accession codes, unique identifiers, or web links for publicly available datasets
- A list of figures that have associated raw data
- A description of any restrictions on data availability

The data and code that support the plots within this paper and other findings of this study are available from the corresponding author upon reasonable request and with permission from corporate collaborations.

Field-specific reporting

Please select the one below that is the best fit for your research. If you are not sure, read the appropriate sections before making your selection.

☒ Life sciences ☐ Behavioural & social sciences ☐ Ecological, evolutionary & environmental sciences

Life sciences study design

All studies must disclose on these points even when the disclosure is negative.

Sample size	Described in Methods section, "Differential measurement calculation".
Data exclusions	Not applicable.
Replication	All attempts at replication were successful.
Randomization	Not applicable.
Blinding	Investigators were not blinded to group allocation.

Reporting for specific materials, systems and methods

We require information from authors about some types of materials, experimental systems and methods used in many studies. Here, indicate whether each material, system or method listed is relevant to your study. If you are not sure if a list item applies to your research, read the appropriate section before selecting a response.

Materials & experimental systems

n/a	Involved in the study
☒	☐ Antibodies
☐	☒ Eukaryotic cell lines
☒	☐ Palaeontology
☐	☒ Animals and other organisms
☒	☐ Human research participants
☒	☐ Clinical data

Methods

n/a	Involved in the study
☒	☐ ChIP-seq
☒	☐ Flow cytometry
☒	☐ MRI-based neuroimaging

Eukaryotic cell lines

Policy information about cell lines

Cell line source(s)	B16 mouse skin melanoma cell line from American Type Culture Collection (ATCC).
Authentication	The B16 cell line used was authenticated by ATCC before it was delivered to us.
Mycoplasma contamination	The B16 cell line was tested for mycoplasma contamination by ATCC.
Commonly misidentified lines (See ICLAC register)	No commonly misidentified cell lines were used.

Animals and other organisms

Policy information about studies involving animals; ARRIVE guidelines recommended for reporting animal research

Laboratory animals	Female Swiss Webster mice (Hsd: ND4, Envigo)
Wild animals	No wild animals were used.
Field-collected samples	No sample was collected from the field for this study.
Ethics oversight	All the laboratory animal protocols were approved by the Animal Studies Committee of Washington University in St. Louis and the Institutional Animal Care and Use Committee of California Institute of Technology.

Note that full information on the approval of the study protocol must also be provided in the manuscript.